Improving the External Extraction Efficiency of

Organic Light Emitting Devices

by

John C. Ho

S.B., Electrical Engineering and Computer Science
Massachusetts Institute of Technology, 2002

Submitted to the Department of Electrical Engineering and Computer Science

in Partial Fulfillment of the Requirements for the Degree of

Master of Engineering in Electrical Engineering and Computer Science

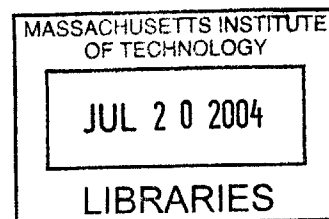at the Massachusetts Institute of Technology

February 4, 2004 [June 2004]

Author_____
Department of Electrical Engineering and Computer Science
February, 2004

Certified by_____
Vladimir Bulović
Associate Professor
Thesis Supervisor

Accepted by_____
Arthur C. Smith
Chairman, Department Committee on Graduate Theses

i

Improving the External Extraction Efficiency of

Organic Light Emitting Devices

by

John C. Ho

Submitted to the Department of Electrical Engineering & Computer Science
in Partial Fulfillment of the Requirements for the Degree of
Master of Engineering

Abstract

Over the last decade Organic Light Emitting Device (OLED) technology has matured, progressing to the point where state-of-the-art OLEDs can demonstrate external extraction efficiencies that surpass those of fluorescent lights. Additionally, OLEDs have the benefits over conventional display and lighting technologies of large viewing angles and mechanical flexibility. However, in order to become a commercially viable, widely adopted technology, OLEDs must not only match the long-term stability of competing technologies, but must demonstrate a distinct advantage in efficiency. This thesis presents various strategies for fabricating nanopatterned structures that can be integrated into OLEDs with the aim of improving the external extraction efficiency. Soft nanolithography, colloidal deposition, and preparation of metallic nanoparticle films are among the fabrication techniques investigated for potential applications in enhancing OLED performance.

Thesis Supervisor: Vladimir Bulović
Title: Associate Professor of Electrical Engineering and Computer Science

TABLE OF CONTENTS

LIST OF FIGURES

v

ACKNOWLEDGMENTS

GLOSSARY

Anode – A positively charged electrode that is the source of holes, or the sink of electrons, in an electrical device.

Anthracene – A crystalline solid that can range in hue from colorless to pale yellow. One of a group of chemicals called **polycyclic aromatic hydrocarbons (PAHs)**. The chemical structure is shown below:
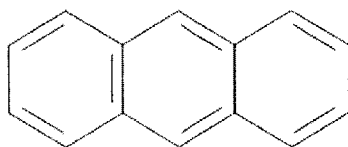
Cathode – A negatively charged electrode that is the source of electrons, or the sink of holes, in an electrical device

Conjugation – The presence of alternating double (or triple) and single bonds between carbon atoms in a chemical compound.

Electron – A sub-atomic particle with a quantized negative charge.

Electron-Volt (eV) – A unit of energy, typically used to measure energy of atoms, molecules, or individual photons. A useful conversion factor is

$$\frac{1241\, eV \cdot nm}{x}, \text{ where x is in eV.}$$

Exciton – An exciton is a combination of an electron and a hole in a semiconductor or insulator in an excited state. The hole behaves as a positive charge, and the electron is attracted to it to form a state similar to a hydrogen atom. The probability of the electron falling into the hole is limited by the difficulty of losing the excess energy, so that the exciton may have a relatively long life. Alternatively, an exciton may be thought of as an excited state of an atom or ion, the excitation wandering from one cell of the lattice to another.

Hole – The absence of an **electron** in a semiconductor material, which can be modeled as positive charge carriers in an electrical device.

Intrinsic Carrier Concentration – The formula for calculating intrinsic carrier concentration at thermal equilibrium is

$$n_i = N_s e^{\left(-\frac{E_g}{2k_B T}\right)}$$

where:

- n_i is the intrinsic carrier concentration per unit volume in a semiconductor free of defects or impurities.
- N_s is the number per unit volume of effectively available states.
- E_g is the energy gap between the LUMO and the HOMO.
- k_B is the Boltzmann's constant, 1.381×10^{-23} Joules/Kevin.
- T is the absolute temperature in Kelvin.

Ohmic Contact – A metal-semiconductor contact that has a linear or near-linear current-voltage characteristic

Polycyclic Aromatic Hydrocarbons (PAHs) – A group of highly reactive organic compounds. Hydrocarbons refer to organic compounds containing only carbon and hydrogen. Aromaticity refers to a configuration of six carbon atoms into a planar ring that are connected by delocalized electrons. The simplest aromatic hydrocarbon is known as a benzene ring (Figure below). Polycyclicity refers to the presence of multiple carbon rings in a compound.
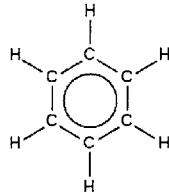
Vacuum Level – The energy level of a free electron

Work Function – The minimum energy required to transfer an electron from the Fermi level within a solid to a point just outside its surface.

C h a p t e r 1

INTRODUCTION TO ORGANIC LIGHT EMITTING DEVICES (OLEDS)

A Brief History of Organic Electroluminescence (EL) Research

Research on the generation of light from organic materials began as early as the 1950's. In the

early 1960's, researchers, such as M. Pope [1] and W. Helfrich [2], worked on single crystals of

anthracene to achieve light-emitting devices. However, there were several drawbacks

preventing practical use of these early devices including low light output, high operational

voltages, and unstable materials. The high operating voltages were a result of the crystal

thicknesses in the micrometer (1×10^{-6} m) range along with difficulties reproducing crystal

growth as well as poor electrical contacts.

The next step in the evolution towards efficient OLEDs was made in the 1970s through the

use of vacuum vapor deposition techniques to prepare thin organic films. The reduction of

the organic layer thickness well below 1 micron allowed researchers to achieve electric fields

comparable to those applied to single crystals, but at a considerably lower voltage. But,

research was shelved again due to the inability to produce thin, morphologically smooth

organic films; defects such as pin-holes resulted in unstable device operation.

Finally, in the late 1980's C.W. Tang [3] and J.H. Burroughes [4] demonstrated OLEDs with

the potential for lighting and display applications. Their works utilized organic films deposited

by thermal evaporation or spin-coating, leading to thin (1×10^{-9} m), smooth, and

homogeneous films. The small thicknesses led to low operating voltages (~ 10 V), which were compatible with modern electronics. The homogeneous films led to high dielectric strength and the possibility of applying large electric fields. Their deposition methods also made large area devices possible. However, it was their development of the multi-layer OLED structure that let to considerable improvements in efficiency of light emission by achieving a better balance of charge carriers (**holes** and **electrons**) and improving the electrical contact between the organic layers and the electrodes. This breakthrough sparked efforts in the development of new molecular materials and device structures. Over the last decade, OLEDs have entered the commercial world through cell phones, car stereos, and digital cameras and are considered as promising candidates for future display and lighting applications.

OLED Device Structure

A typical OLED consists of organic layers that are sandwiched between two electrodes and are many times thinner than a sheet of paper. Figure 1.1a presents a cross-section of a canonical green OLED, which is the basis for all of the experiments in this thesis. Each layer in the OLED serves a unique purpose, and for that reason choosing the appropriate thickness and material of each layer is crucial. The **cathode** is typically made of a Magnesium-Silver (Mg/Ag) alloy. For reasons discussed later, the cathode must have a low **work function (W)**; however, such materials are quite reactive. Choice materials are presently Calcium (W ≈ 2.87 eV) and Mg/Ag (W ≈ 3.6 eV). The next layer down is the organic layer, which consists of different materials depending on the desired color. Because the organic light emission is typically in the visible range, a photon energy from 1.7 eV to 3.1 eV is required. This

necessitates the use of **conjugated** molecules or polymers in the emitting layer, whose lowest unoccupied molecular orbitals (LUMOs) and highest occupied molecular orbitals (HOMOs) are typically 2-3 eV and 5-6 eV below **vacuum level**. The presence of conjugation also results in semiconducting organic materials that can respond to electrical signals. For all of the devices in this thesis, a tris-(8-hydroxyquinoline) aluminum (Alq₃) and an N,N'–diphenyl-N,N'-bis(3-methylphenyl)1-1'biphenyl-4,4'diamine (TPD) heterojunction was used as the active organic layer (see Figure 1.1b). Underneath the organic layer lies the **anode**, which is composed of a thin layer of Indium Tin Oxide (ITO). ITO is a conveniently transparent, conductive material, through which the emitted light escapes the device. For reasons discussed below, the anode requires a rather large work function, and ITO, depending on the surface treatment, can have a work function between 4.7 eV and 4.9 eV. Finally, all of these layers are vacuum-deposited onto a transparent substrate, which is typically glass.
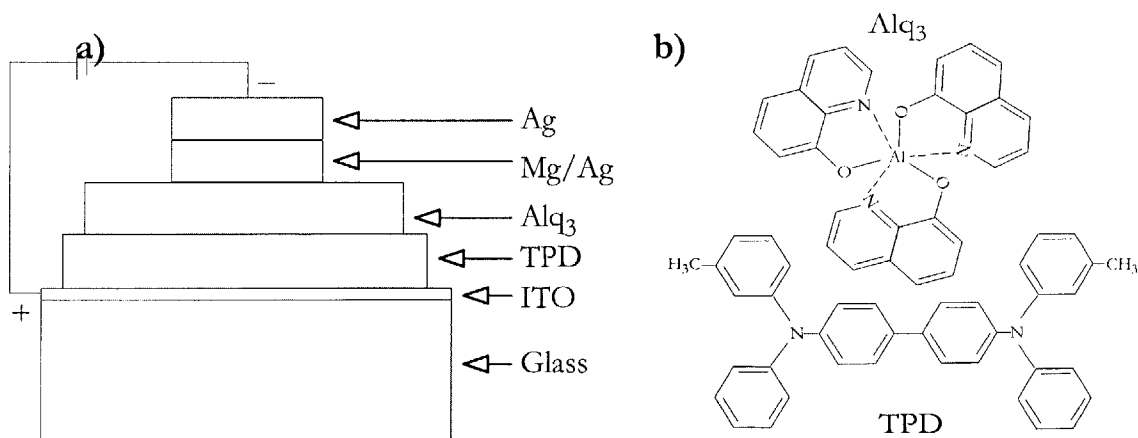
Figure 1.1. a) Cross-sectional view of a typical green OLED b) Chemical structures of Alq3 and TPD

OLED Device Operation

Electroluminescence (EL) is the generation of light from matter using electricity and is at the core of OLED operation. In order to better understand the EL process researchers use a simple energy band model to describe OLED behavior (see Figure 1.2). A typical I-V curve for a green OLED is shown in Figure 1.3. From the energy band model it becomes easier to relate the I-V characteristics with the basic processes required for EL in organic solids: charge carrier injection, charge carrier transport, **exciton** formation, emission of a photon, and transport of the photon out of the device.
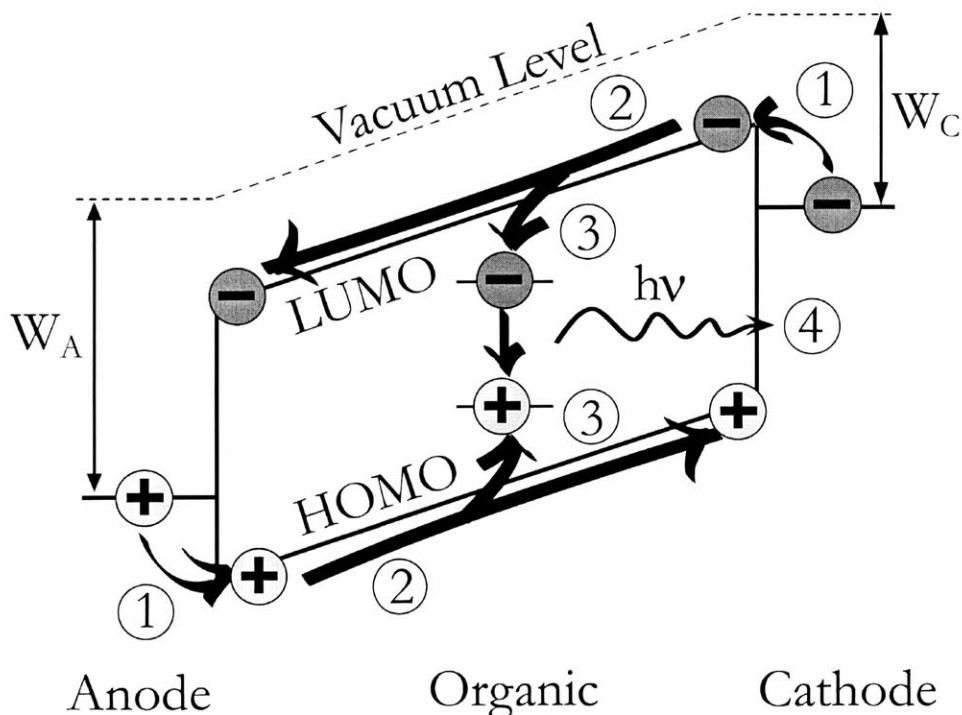
Figure 1.2. Simplified energy band diagram representing the basic steps of EL: (1) charge carrier injection, (2) charge carrier transport, (3) exciton formation, and (4) radiative exciton decay. (W_C: cathode work function, W_A: anode work function).
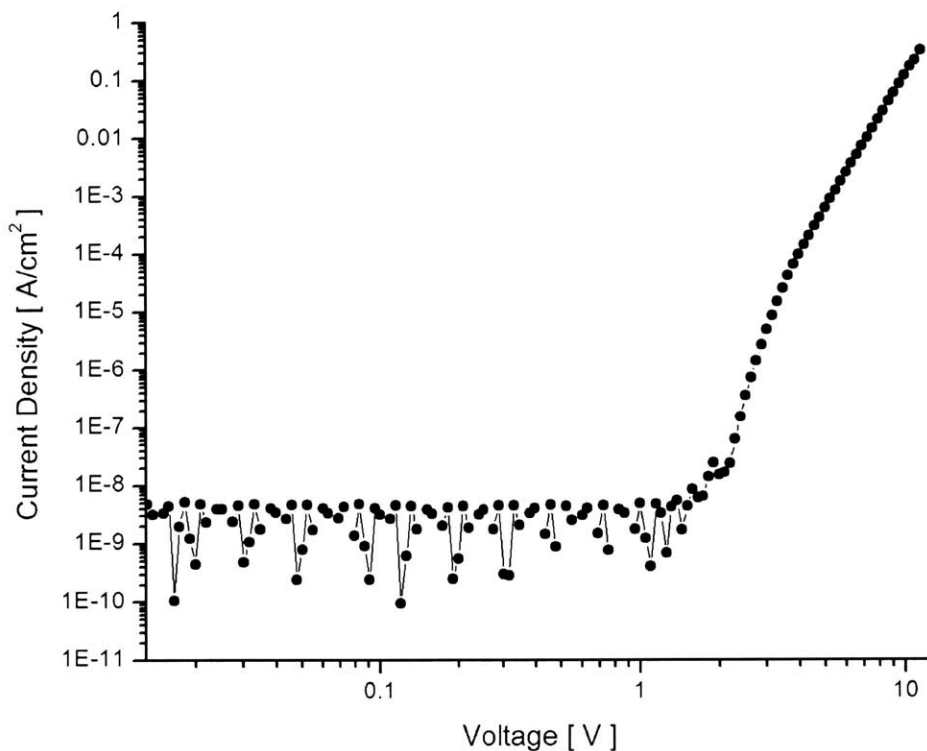
Figure 1.3. A characteristic I-V curve for a standard, green OLED with the following layers, TPD:Alq3:Mg/Ag:Ag (500 Å: 500 Å: 500 Å: 500 Å).

Charge Carrier Injection and Transport

Many of the materials in OLEDs are wide-gap materials with energy gaps of 2 to 3 eV. Thus, the **intrinsic carrier concentration** in the organic materials is very small ($< 10^{-10}$ cm^3). From this perspective, it is appropriate to consider the materials more as insulators than semiconductors. Any charge carriers present in the operating OLED must be injected from the electrodes. Generally, the relative positions of the energy levels in the organic films and the metal electrodes create energy barriers for injection.

Once carriers are injected into the organic material, they are transported by the applied electric field towards their respective electrodes. Because of the disorder inherent in organic materials, charge carrier transport in organic materials is described by hopping between localized, molecular sites with different energy and distance. Additionally, carriers can be trapped in gap states originating from impurities or structural traps. This results in low carrier mobilities, which are typically between 10^{-3} and 10^{7} $cm^2/V \cdot s$ at room temperature. Research suggests that conduction in OLEDs is consistent with a trapped-charge-limited (TCL) model [5].

Carrier Recombination

If enough voltage is supplied to the OLED, the electrodes will induce an electric field that injects electrons from the cathode (Mg-Ag) and holes from the anode (ITO). If both charges arrive on a single organic molecule, a molecular excited state may be formed. The Coulombic interaction between the closely spaced charge carriers creates a large binding energy for the molecular excited state. Thus, the molecular excited state cannot be dissociated easily, and its properties are conserved, over a finite lifetime. This molecular excited state diffuses through the organic layer between molecules, allowing it to be treated as a particle known as an exciton.

Exciton Decay and Light Out-coupling

An exciton can be classified as either a singlet or a triplet based on its spin. Singlet excitons quickly and efficiently decay, emitting light in a process known as fluorescence. Triplet excitons, however, have a low probability of luminescence and almost always decay in slower, non-radiative processes. The wavelength of the emission depends on the energy bandgap of the emissive material, and the intensity of the light is proportional to the current. Light is

generated in the organic layers within the OLED, however not all of the light is able to escape the device. Much of the light is waveguided within the layers of the OLED due to total internal reflection. One important figure of merit for determining how much light leaves the device is the output coupling efficiency or external extraction efficiency, which is defined as the ratio of the number of photons emitted by the OLED into the viewing direction to the number of electrons injected. Three different fabrication techniques are explored in this thesis: nanolithography, colloidal deposition, and metallic nanoparticle deposition. These techniques lay the foundation for creating new device structures that have the possibility of improving the output coupling efficiency of OLEDs.

Chapter 2

APPROACHES FOR MODELING AND EXTRACTING WAVEGUIDED LIGHT

Extracting the waveguided light that is trapped within OLEDs is the main thrust of this thesis, and in the next few sections the motivations for this research will become clear. To have any hopes of controlling the waveguided light, we need to first take a closer look at where the generated light is going.

Quantum Efficiency

The quantum efficiency, η_Q, of an OLED is an important figure of merit for devices and can be experimentally measured. Quantum efficiency is defined as the number of photons exiting the device per injected electron and can be expressed as a product of the fraction of emissive excitons, χ; the photo luminescent efficiency of the emissive molecule, ϕ_{PL}; and the output coupling efficiency, η_X :

$$\eta_Q = \chi\eta_X\phi_{PL} \tag{EQ 2.1}$$

A sample quantum efficiency vs. current curve is shown in Figure 2.1. The singlet to triplet ratio produced by conventional OLEDs has been directly measured to be approximately 1:3. Thus, the fraction of emissive excitons, χ, in a fluorescent OLED is restricted to 25%. However, through a technique called electrophosphorescence [6], OLEDs can be made to

efficiently harvest the energy from triplet excitons to produce light, effectively making χ close to 100%.
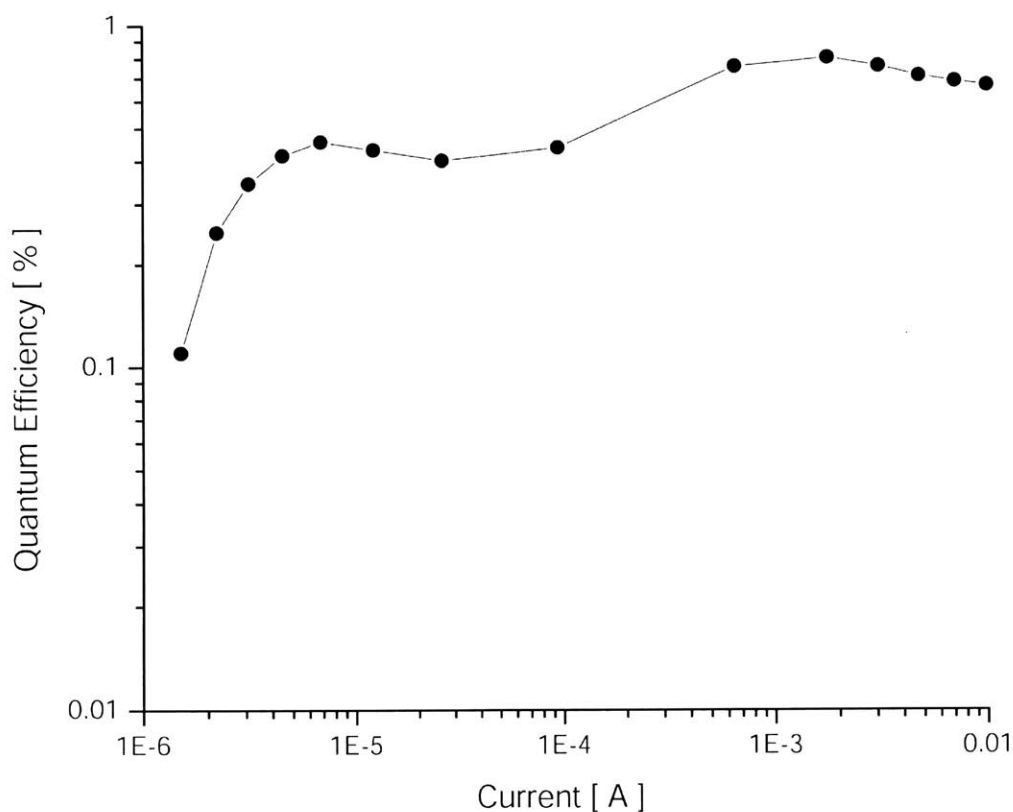
Figure 2.1. A sample external quantum efficiency vs. current graph taken from a standard, green OLED with the layers TPD:Alq3:Mg/Ag:Ag (500 Å: 500 Å: 500 Å: 500 Å).

Additionally, the photo-luminescent efficiency, ϕ_{PL}, of a molecule under optical excitation is defined as the number of emitted photons per absorbed photon. Device optimizations such as creating a heterojunction with an electron transport layer (ETL) and a hole transport layer (HTL) in conjunction with electrophosphorescence have also made ϕ_{PL} close to 100%.

Because it is possible to make both ϕ_{PL} and χ close to 100%, the only remaining limitation to the quantum efficiency of OLEDs is the output coupling efficiency, η_X. The structural and physical properties of OLEDs directly limit η_X through absorption losses and by waveguiding light within the layers of the device. Traditional OLEDs tend to harness approximately 20% of the total light emitted from an organic light source [7]. As the light is emitted from the organic layer it travels in all directions. Because of the changes in the index of refraction from layer to layer, the light emitted from the source will refract. Some of the light will refract so much that it becomes trapped in any one of the layers due to total internal reflection. Also, light that is reflected back through the device has a large probability of being absorbed by the organic molecules or the metal electrode. Thus, a large portion of the light created never makes it out of the viewing surface and goes to waste.

Ray Optics Model

By ignoring microcavity effects, assuming that there is no diffuse scattering at interfaces, and approximating all surfaces to be planar we can build a model to estimate just how much light gets trapped in an OLED structure based on simple geometry. Despite not accounting for the quantum mechanical microcavity effects, it is still possible to arrive at a relatively accurate estimate of the distribution of waveguided light within the device. First, we require an understanding of Snell's Law, which is a direct result of Fermat's principle, stating that a beam of light travels the path between two points in space that requires the least amount of time:

$$n_1 \sin \theta_1 = n_2 \sin \theta_2 \qquad \text{(EQ 2.1)}$$

Snell's law applies light that is incident on an interface between layers with different **indices of refraction** (see Figure 2.2).
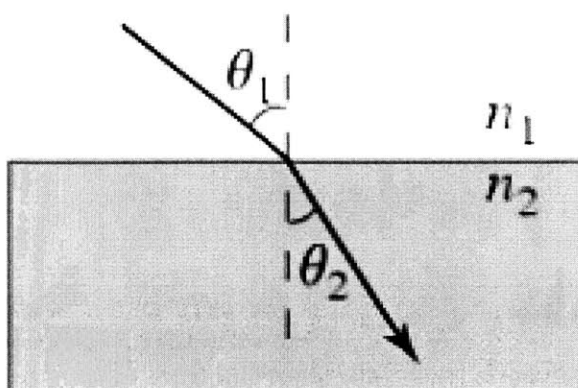
Figure 2.2. A schematic demonstration of Snell' law with two layers that have different indices of refraction n_1 and n_2. θ_1 is the incident angle of the light and θ_2 is the refracted angle.

With Snell's law we can begin to look at waveguiding in the OLED structure layer by layer. Assuming an isotropically light-emitting point source (i.e. an Alq_3 molecule), only the rays contained in a right-circular cone defined by the critical angle (θ_C) can escape from layer 1 (emitting layer) to layer 2 (receiving layer):

$$\theta_{C,1 \to 2} = \arcsin\left(\frac{n_2}{n_1}\right)$$ (EQ 2.2)

A ray diagram of the various optical paths taken in an OLED is shown in Figure 2.3.
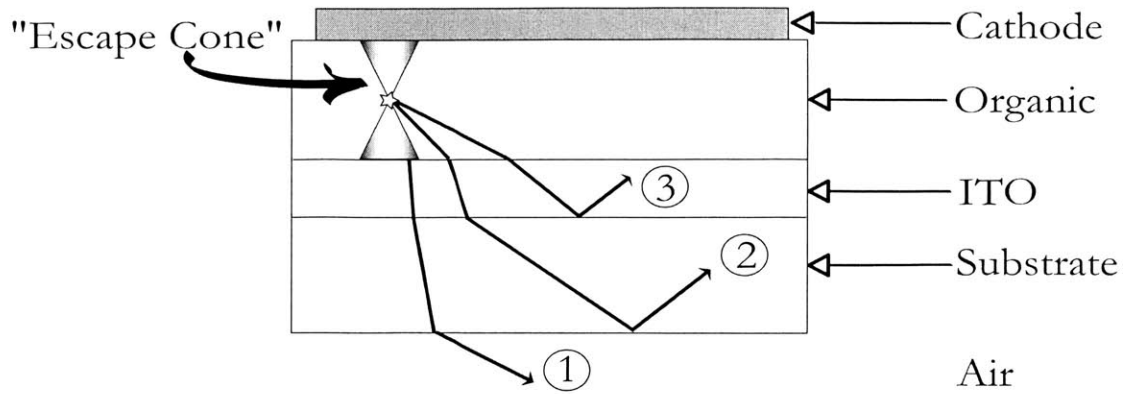
Figure 2.3. A schematic diagram of optical paths in an OLED. Only light emitted at angles within the "escape cone" will leave the device (ray 1). Light emitted at larger angles results in trapping in the substrate (ray 2) and in the organic/anode layers (ray 3).

$\theta_{C(org-air)}$ is the critical angle between the organic layer and air. Furthermore, the fraction of

light trapped in the substrate, η_{sub}, and the organic/ITO layers, $\eta_{org/ITO}$, are given by

$$\eta_{sub} = \cos\theta_{C(org-air)} - \cos\theta_{C(org-sub)} \qquad \text{(EQ 2.4)}$$

$$\eta_{org/ITO} = \cos\theta_{C(org-sub)} \qquad \text{(EQ 2.5)}$$

where $\theta_{C(org-sub)}$ is the critical angle between the organic layer and the substrate. For glass

substrates and typical indices of refraction for the organic (n ~ 1.7) and ITO (n ~ 1.8 -2.1)

layers, the external extraction efficiency, η_{ext}, is only approximately 17%. Close to 51% of the

light is waveguided in the organic/ITO layers and the remaining 32% of the light remains

trapped in the substrate layer [7].

Notable Approaches

By looking at previous work on improving the outcoupling efficiency of OLEDs, it becomes easier to see the best approach to solving this problem. A variety of techniques have demonstrated an increase in the output coupling efficiency. One solution to the light trapping problem is to add a spherical glass lens the substrate of the OLED [8]. This approach did improve the external extraction efficiency by a factor of 3. However, the spherical lens needs to be relatively large in size compared to the thickness of the actual OLED pixel because the focal point of the lens is pushed further away by the device layers in between, making this scheme inappropriate for integration into displays.

Alternatively, an ordered microlens array was placed on the substrate and achieved a 50% increase in external extraction efficiency over a flat, glass substrate [9]. While this solution could be used in lighting and display applications, the difficult process of fabricating microlens arrays prohibits this technique from gaining widespread use in manufacturing.

Finally, a two-dimensional photonic crystal was patterned onto the inner surface of an OLED substrate [10]. Experimentally, a 50% enhancement of the external extraction efficiency over a conventional OLED was observed. However, the far-field intensity profile of the photonic-crystal OLED (PC-OLED) exhibited a pattern attributable to the photonic-crystal pattern. This makes integration in display applications much more difficult. Also, there was no data shown for the effect of the PC-OLED on the spectrum of the emitted light. Presumably, the broad emission spectrum of organic materials would exceed the photonic bandgap and therefore interact with the photonic crystal to change the spectrum of the emitted light. The

processing required to fabricate the 2-D photonic crystals prevents this technique from widespread use as well.

Scattering Waveguided Light

One aspect that all of the previous approaches had in common, was that the patterning was applied to a face of the substrate. This has the disadvantage of putting the optically active elements farther away from the emissive layer. If the distance between the patterning and the light-emitting layer could be made smaller the size of the patterned features can be minimized. My solution to the efficiency problem is motivated by the need to move the optically active layer as close as possible to the light-emitting layer and by the need to keep the processing of organic devices as simple as possible. The idea is to create scattering centers that will be as close as possible to the organic layer without changing the electrical properties of the OLED. Performing a simple calculation, we can estimate the possible gains in external extraction efficiency from this approach.

Ray Optics Analysis of Light Scattering

Considering a simple isotropic emitter and an adjunct, scattering layer it is possible to reasonably estimate the potential improvements in outcoupling efficiency. For simplicity, assume a square device profile as shown in Figure 2.4.
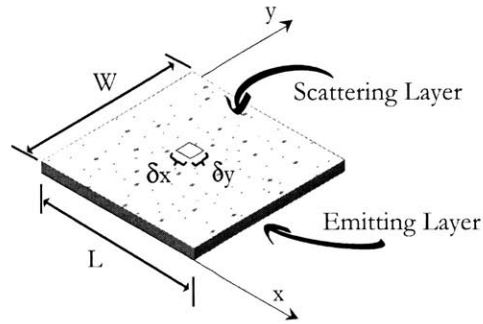
Figure 2.4. A simplified device containing only a scattering and emissive layer.

Using geometry, we can calculate the critical angles in the x and y dimension for light to escape

the scattering layer (Figure 2.5).
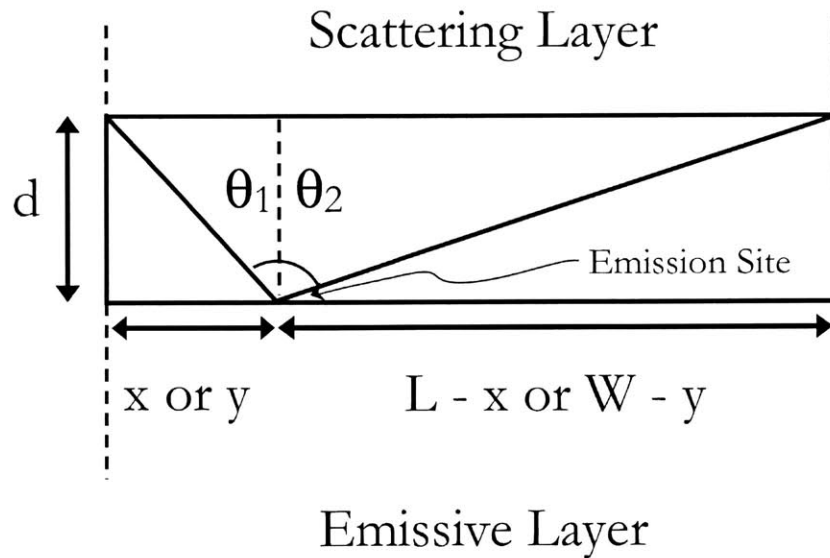
Figure 2.5. A diagram illustrating the geometry of the escape angle. The only photons that matter are the ones that leave the front of the device through the scattering layer.

Assuming the scattering layer is placed some distance, d, away from the emissive layer, then

the equations determining the escape cone are

$$\theta_x(x) = \theta_{1,x} + \theta_{2,x} = \tan^{-1}\left(\frac{x}{d}\right) + \tan^{-1}\left(\frac{L-x}{d}\right) \qquad \text{(EQ. 2.6)}$$

$$\theta_y(y) = \theta_{1,y} + \theta_{2,y} = \tan^{-1}\left(\frac{y}{d}\right) + \tan^{-1}\left(\frac{W-y}{d}\right) \qquad \text{(EQ. 2.7)}$$

By assuming we have an isotropic emitter, we can integrate over the device area and normalize over the device dimensions to obtain the fraction of forward emitted light that reaches the scattering layer, η:

$$\eta = \frac{1}{A}\int_A \frac{\theta_x(x)}{\pi}\frac{\theta_y(y)}{\pi}\,dA \qquad \text{(EQ. 2.8)}$$

Remembering that the device is square and L is equal to W, we can further simplify the expression:

$$\eta = \frac{1}{\pi^2}\cdot\frac{1}{L^2}\left[\int_0^L \theta_x(x)\,dx\right]^2 = \frac{1}{\pi^2}\cdot\frac{1}{L^2}\left[\int_0^L \tan^{-1}\left(\frac{x}{d}\right) + \tan^{-1}\left(\frac{L-x}{d}\right)dx\right]^2$$

$$= \frac{1}{\pi^2}\cdot\frac{1}{L^2}\left[2\int_0^L \tan^{-1}\left(\frac{x}{d}\right)dx\right]^2 \qquad \text{(By device symmetry)}$$

$$= \frac{1}{\pi^2}\cdot\frac{1}{L^2}\left\{2\left[x\tan^{-1}\left(\frac{x}{d}\right) - \frac{d}{2}\ln\left(d^2 + x^2\right)\right]_0^L\right\}^2$$

$$= \frac{4}{\pi^2 L^2}\left[L\tan^{-1}\left(\frac{L}{d}\right) - \frac{d}{2}\left(\ln\left(d^2 + L^2\right) - \ln\left(d^2\right)\right)\right]^2$$

$$L \tan^{-1}\left(\frac{L}{d}\right) \approx \frac{L\pi}{2} \quad \text{and} \quad \frac{d}{2}\ln\left(\frac{d^2+L^2}{d^2}\right) \approx \frac{d}{2}\ln\left(\frac{L}{d}\right) \to 0 \qquad \text{(For } d \ll L\text{)}$$

$$\therefore \eta = 1$$

Thus, in the limit that the scattering layer is placed directly adjacent to the emissive layer all of the light will reach the scattering layer.

Assuming purely random (memoryless) scattering and considering the lower limit of scattering effects (i.e. no contribution from secondary reflections) 50% of the light that reaches the scattering centers will be scattered in the forward direction. Secondary reflections have the potential to further improve the external extraction efficiency as backscattered light is reflected off the cathode into the forward direction. Absorption will reduce this contribution, and diffusion of the light away from the device area will negatively impact display resolution. However, diffusion of the light away from the device will be negligible assuming the light is traveling in a film that is much thinner than its lateral dimensions. Also, absorption can be effectively ignored based on simulations documented in Chapter 4.

Thus, assuming a cathode that is ~80% reflective [13] at 530 nm (wavelength of green light), including secondary reflections, and ignoring absorption effects we can estimate the total fraction of light that is scattered forward out of the emissive layer (organic/ITO) to be

$$\eta_{total} = \sum_{j=1}^{\infty}(0.5)^{j}(0.8)^{j-1} \to 1 \qquad \text{(EQ. 2.9)}$$

So, we arrive at the approximation that all of the emitted light will eventually scatter forward into the next layer. This next layer will be glass in all of the experimental device structures explored in this thesis. Thus, the index of refraction difference between the glass substrate (n = 1.5) and air (n = 1.0) will result in a fraction of the emitted light getting externally extracted. This fraction becomes the external extraction efficiency, η_{ext}, and can easily be calculated from Snell's law by finding the critical angle for light traveling through glass into air:

$$\theta_{C,glass-air} = \sin^{-1}\left(\frac{n_{air}}{n_{glass}}\right) = \sin^{-1}\left(\frac{1}{1.5}\right) \approx 41° \qquad (EQ.\ 2.10)$$

Thus, external extraction efficiency becomes approximately $41°/90° \times 100\% \approx 45\%$, resulting in a factor of 2.5 improvement over the calculated external extraction efficiency of conventional OLEDs.

Proposed Device Structures

By using microsphere monolayers and metallic nanoparticles as scattering centers we have a couple of potential solutions that will be capable of being integrated into any device structure and will produce a significant factor of improvement in external extraction efficiency. Microsphere deposition can result in devices that have the structure illustrated in Figure 2.6. The microspheres will lie between the ITO and the glass substrate, which means that ITO will be sputtered on top of the microspheres after they are deposited onto glass. Effectively, this will cause the ITO to conform to the pattern formed by the lattice of microspheres thereby roughening the ITO and causing it to become a scattering layer. The metallic nanoparticles are

another scattering media that can be used to roughen the surface of the ITO. The processing would only require a few angstroms of metal evaporated onto the ITO coated glass substrate. This would again have the effect of roughening the ITO and organic interface, letting the emitted light scatter into the glass substrate.
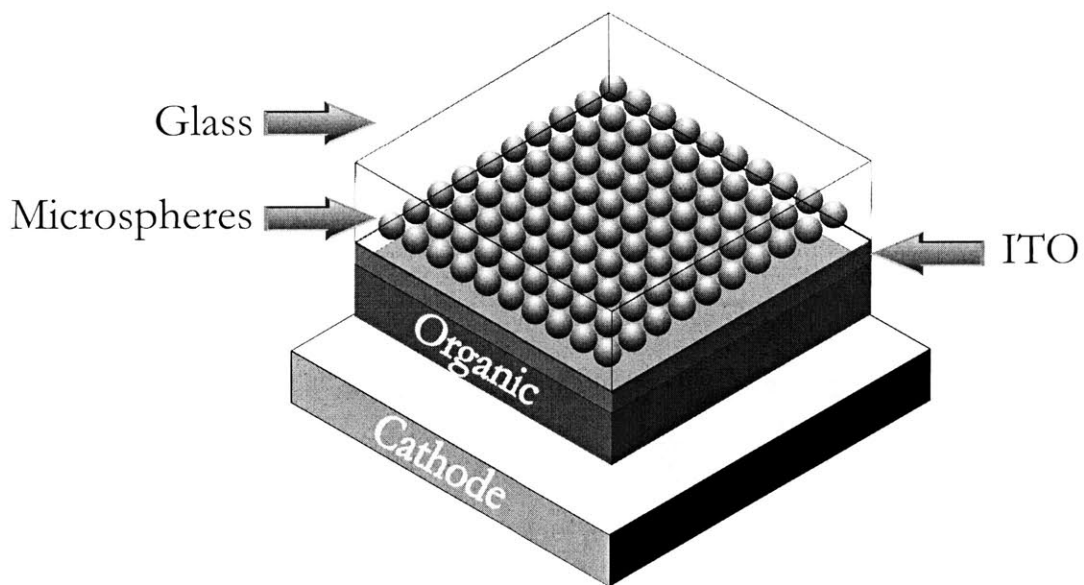
Figure 2.6. A schematic of a proposed device structure that incorporates microspheres as a form of scattering media.

C h a p t e r 3

EXPERIMENTAL METHODS

While not all of the fabrication techniques described in this section may appear to be directly related to OLEDs, the methods may, in the future, play a role in realizing a more efficient OLED. The detailed processes of nanopatterning PDMS, microsphere deposition, and metallic nanoparticle evaporation are explained below.

Fabrication of 2-D Periodic Nanostructures in Poly(dimethylsiloxane) (PDMS)

There are two fabrication processes that are required to construct periodic nanostructures in PDMS: Interference Lithography and Soft Lithography. Figure 3.1 steps through the whole process, showing how both fabrication processes are combined to create the final, structured PDMS film. The sections below will explain each fabrication process in detail.

Interference Lithography

Interference Lithography (IL) is a patterning technique that can create sub-micron features that are periodic over a large area (usually several centimeters). IL allows vast numbers of identical structures to be patterned with short exposure times and simple equipment. The periodic pattern is formed by the constructive and destructive interference of light waves that form a standing wave at the surface of the substrate, which is covered with a layer of light-sensitive photoresist. This standing wave exposes the photoresist, allowing the periodicity of the standing wave to be transferred to the photoresist layer. The period of the transferred

pattern, P, is a function of the source wavelength (λ) and the angle between the normal to the substrate surface and the light beams (θ) [11]:

$$P = \frac{\lambda}{2 \sin \theta}$$

(EQ. 3.1)
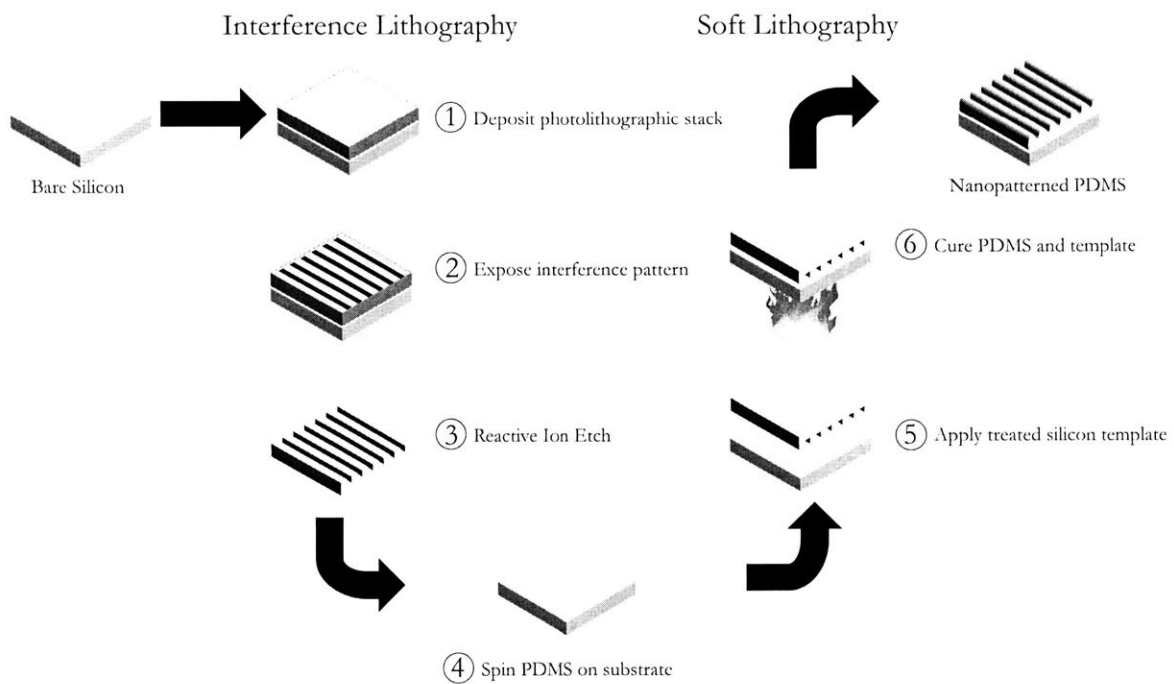
Figure 3.1. A diagram of the processes involved in fabricating thin, nanopatterned PDMS films. Interference lithography consists of steps 1-3 and soft lithography consists of steps 4-5.

Lloyd's Mirror Interferometer

The Nanostructures Laboratory (NSL) is home to the Lloyd's Mirror IL system, which was used to create all of the structures documented in this thesis. The Lloyd's Mirror Interferometer uses a broad laser beam and a mirror to generate the interference patterns on the substrates as shown in Figure 3.2. The mirror is held perpendicular to the substrate

surface and uses the incident beam to create a second beam that generates the interference

pattern. The period of the grating will be determined by Equation 3.1, where θ is determined

by the orientation of the mirror and substrate with respect to the incident beam.
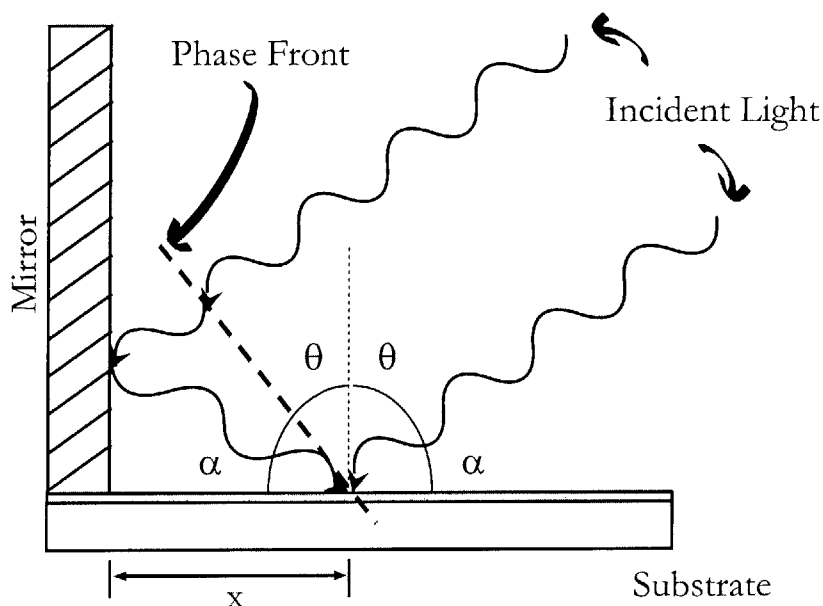
Figure 3.2. Schematic of basic Lloyd's Mirror configuration, generating an optical path length difference.

The Lloyd's Mirror system, as illustrated in Figure 3.3, uses a 54 mW helium cadmium (HeCd)

ultraviolet laser at a wavelength of 325 nm as the light source. The mirror and the substrate

are rigidly attached to the substrate holder via vacuum suction. The substrate holder rests on a

rotation stage which can change the incident angle of the laser beam on the mirror and the

substrate, reliably setting the period of the grating anywhere from 200 nm to 1000 nm. A

spatial filter is used to remove the high frequency noise from the laser beam before exposing

the photoresist, creating an approximately Gaussian beam profile. A pinhole is placed

between the spatial filter and the substrate to allow the laser beam diameter to expand so that

it exposes a large area when it finally reaches the surface of the substrate.

HeCd Laser

Mirror

Mirror

Pinhole

Spatial Filter

Substrate Holder
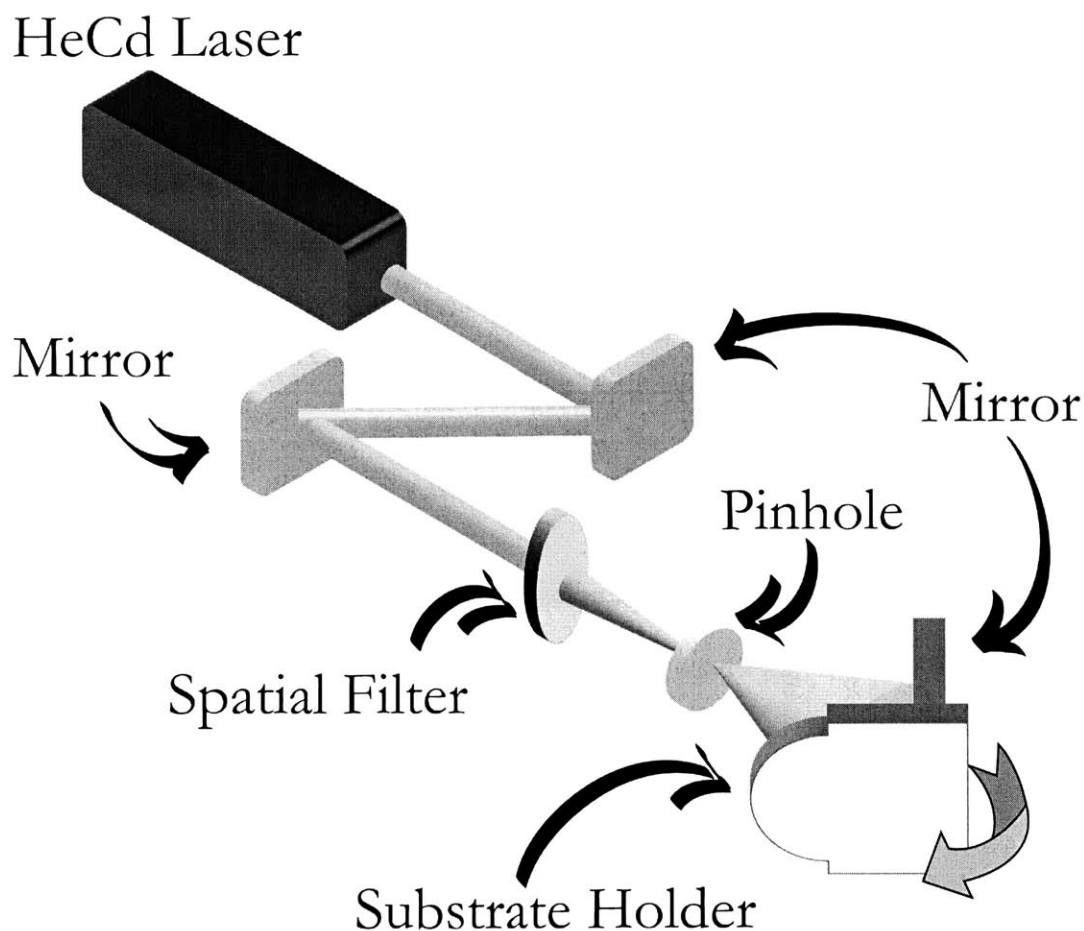
Figure 3.3. An isometric view of the Lloyd's Mirror Interferometer system showing light incident upon both the mirror and substrate. The light reflected off the mirror interferes with the incident light to for a periodic pattern. The rotation stage sets the period by changing the orientation of the mirror and substrate.

The Lloyd's Mirror system is fairly robust and immune to external mechanical vibrations.

Vibrations that affect the relative path length of the two interfering beams are the only

vibrations that affect the exposed pattern. The whole system rests on a floated optical bench,

and the separation of the laser beam does not occur until it reflects off of the mirror, which is rigidly connected to the substrate holder. As a result, relative changes to the beam path lengths are minimized. Also, the period of the grating can easily be adjusted by rotating the mirror/substrate, which changes the angle of incidence. No additional alignment steps are necessary.

However, there are still some drawbacks to using the Lloyd's Mirror system. First, the laser source does not maintain the same power output between exposures. This makes it extremely difficult to properly dose the substrate, usually requiring a process of trial and error to discover the appropriate exposure time. Also, the power of the incident beam is not constant over the area of the spot of the beam, where the edges of the beam are less intense than at the center of the beam. This results in uneven dosing across a substrate, which can drastically reduce the useable area on substrates that require multiple exposures. Gratings with two dimensions of periodicity will require two exposures that are performed at different angles around the axis normal to the substrate, while maintaining the same incident beam angle. There is no rotation stage in the setup that allows for this type of rotation, therefore the substrate must be manually rotated, introducing another source of error and resulting in a lack of precision. Both improper exposure times and rotation angles can result in malformed structures, as illustrated in Figure 3.4.
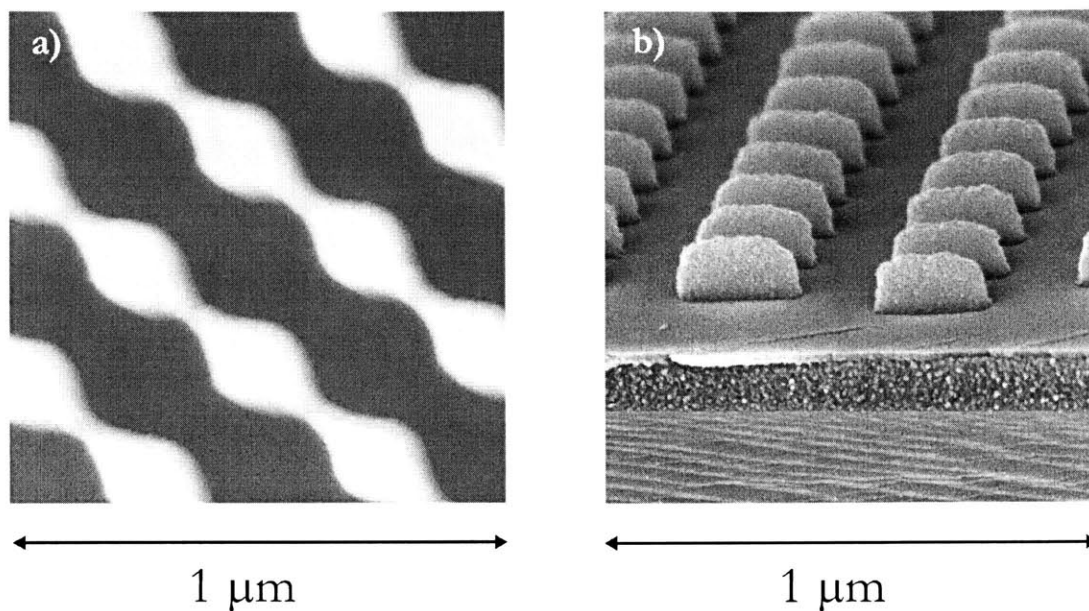
Figure 3.4. a) An AFM image of a photoresist pattern that was underexposed in one of the exposures. b) An SEM image of a photoresist pattern where the angle of rotation between the first and second exposure was too large. In both cases the desired pattern was circular posts in a hexagonal lattice with a period of 300 nm.

Photolithographic Stack

The first step in the process of making a nanopatterned, silicon master template that will act as a mold for the PDMS is to prepare the silicon substrate with a stack. The photolithographic stack refers to the layers of material that are deposited onto a substrate before exposing the sample with an interference pattern.

The bottom of the stack is the Anti-Reflection Coating (ARC). The ARC is a polymer that serves to attenuate the reflections of the incident beam off of the substrate. Light reflected off of the substrate can interfere with the incident beam, forming an interference pattern along the vertical sidewalls of the patterned substrate. This results in a wavy sidewall that may be too

weak to withstand the subsequent development and etching procedures. The reflectivity at any layer boundary in the stack is dependent on the indices of refraction and thicknesses of the stack layers as well as the angle of incidence and wavelength of the laser beam. To minimize the reflected power, a software simulation similar to the one used in [11] is used to determine the necessary ARC thickness based on all of the properties mentioned previously. The software program can calculate the reflectivity at any boundary of the layered stack and can generate a plot of the reflectivity at a specified boundary as a function of ARC thickness. This plot can then be used to determine the proper material and thickness for the ARC. For a 300 nm period grating, typically BARLi ARC is spun at 4000 rpm to achieve a roughly 90 nm thick film. The wafer is then placed on a hot plate at 100° C for one minute to drive off any remaining solvent.

The next deposited layer is a thin film of Silicon Oxide (SiOx), which is thermally evaporated on top of the ARC to act as a hard mask. During the subsequent etching processes the patterned photoresist layer often will not survive for very long. Thus, the SiOx layer is deposited between the photoresist and ARC layers to facilitate deeper etching into the silicon substrate long after the photoresist pattern is gone. For a grating with a period of 300 nm, a 20 nm thick layer of SiOx is deposited.

A thin layer of Hydrogen Dimethyl Sulfoxide (HMDS) is required to provide adhesion between the SiOx layer and the final photoresist layer. Typically a thin film of negligible

thickness is spun on top of the SiOx and then excess solvent is driven off of the substrate at 100° C for a minute on the hot plate.

The final layer in the photolithographic stack is the photoresist, which gets exposed to the interference pattern. When using a positive photoresist, the interference pattern exposes the parts of the surface that will remain after development. When using a negative photoresist, the interference pattern exposes the parts of the surface that will be removed after development. All of the samples in this thesis were fabricated with a desired periodicity of 300 nm. Thus, PFI 88, a negative photoresist, was spun at 4000 rpm to create a 100 nm thick layer. After the photoresist is baked at 100° C for a minute on the hot plate, the substrate is exposed to the interference pattern for the appropriate dosage time. In the negative photoresist, a longer exposure time results in thinner, smaller features, whereas shorter exposure times result in thicker, larger features.

Reactive Ion Etching (RIE)

RIE is a dry etching technique where ions accelerate towards the substrate, reacting with materials at the surface. RIE removes material in a highly directional manner and is used to transfer the developed patterns that resulted from the lithography steps down through the stack into the substrate. Once the interference pattern has been developed in the photoresist layer, a number of different etching steps are necessary to transfer the pattern through the SiOx layer, the ARC layer, and finally into the silicon substrate. Different materials have varying etch chemistries and therefore require different gases in the etching chamber. RIE

processes are based upon a chemical reaction between the etch gas and the substrate, which binds the substrate atoms into a volatile compound. A good indicator of the possible creation of volatile by-products is the boiling point of compounds containing the etch gas and substrate materials. SiOx is etched using a fluorinated gas such as CHF_3 or CF_4. Polymers such as the photoresist and ARC react with a Helium-Oxygen mixture (He/O2). After etching the substrate is ready for use as a silicon master template in patterning PDMS.

PDMS Nanolithography

Soft lithography is a fabrication technique that was pioneered by George Whitesides at the Department of Chemistry in Harvard [12]. The basic idea is that of using polymer stamps to transfer patterns on the sub-micron scale. To create polymer stamps, molds are created that can shape the polymer with sub-micron resolution. While the fabrication of thick polymer stamps (greater than hundreds of microns thick) is a relatively straightforward process, I am interested in creating thin films (< 1 um) of patterned PDMS that can interact with visible light. PDMS is a cross-linking polymer that can be made transparent and cures without volumetric loss, making it a favorable material for fabricating nanopatterned films.

The PDMS used throughout my experiments is manufactured by Dow Corning as Sylgard 186, which comes as a kit with a tub of silicone elastomer and a bottle of curing agent. In order to achieve thin films of PDMS I developed a process that is illustrated in Figure 3.1. The first step is to mix silicone elastomer with the curing agent in a 10:1 ratio by volume. A change in the ratio of silicone elastomer to curing agent results in changes in the rigidity of the cured

PDMS. Making the ratio smaller will make the PDMS firmer, while a larger ratio will make the PDMS more elastic. Once the PDMS has been mixed (approximately 1 minute by hand) to ensure that the silicone elastomer has been totally exposed to the curing agent, the PDMS is set in a vacuum storage box and degassed for approximately 30 minutes. Next, an optional step is to mix the PDMS with a solvent (i.e. chloroform, hexane, etc.) to act as a thinner. Then, the PDMS is spun onto a substrate; the spin speed can vary depending on desired thickness of the film. Next, I take the silicon template and apply a few drops of surfactant (a 5% Micro 90/water solution by volume) and use a nitrogen gun to blow dry the substrate. The surfactant aids in releasing the silicon stamp from the PDMS after curing. Then, I firmly press the silicon template into the uncured PDMS film. While applying pressure, the PDMS and silicon sandwich is then cured on a heating element at 130° C for 5 minutes. Finally, the silicon template is carefully removed using tweezers, and we are left with the thin, patterned PDMS film on a substrate.

Deposition of Silica (SiO_2) and Polystyrene (PS) Microspheres

A number of deposition techniques were evaluated to determine the best way to achieve a monolayer of microspheres over a large area (0.5 in. x0.5 in.). A flat monolayer becomes important for the eventual integration of these optical elements into a working OLED. Microsphere clusters and larger grain boundaries will most likely end up shorting a device, thus limiting these defects becomes a key consideration when evaluating deposition techniques

Spin-Casting

The spin-casting of microspheres is a technique that has the advantage of being a simple, quick process. However, the deposition dynamics are difficult to fully control, and thus in these experiments I was looking for general trends based on spin speeds, type of solvent, material of sphere, the concentration of spheres, and the size of spheres. The substrates are cleaned using the standard Laboratory of Organic Optics and Electronics (LOOE) cleaning procedure [9] and then placed on the vacuum chuck of the spinner. Then, a couple of drops of solution containing microspheres are spun off the surface at speeds ranging from 1000-6000 rpm.
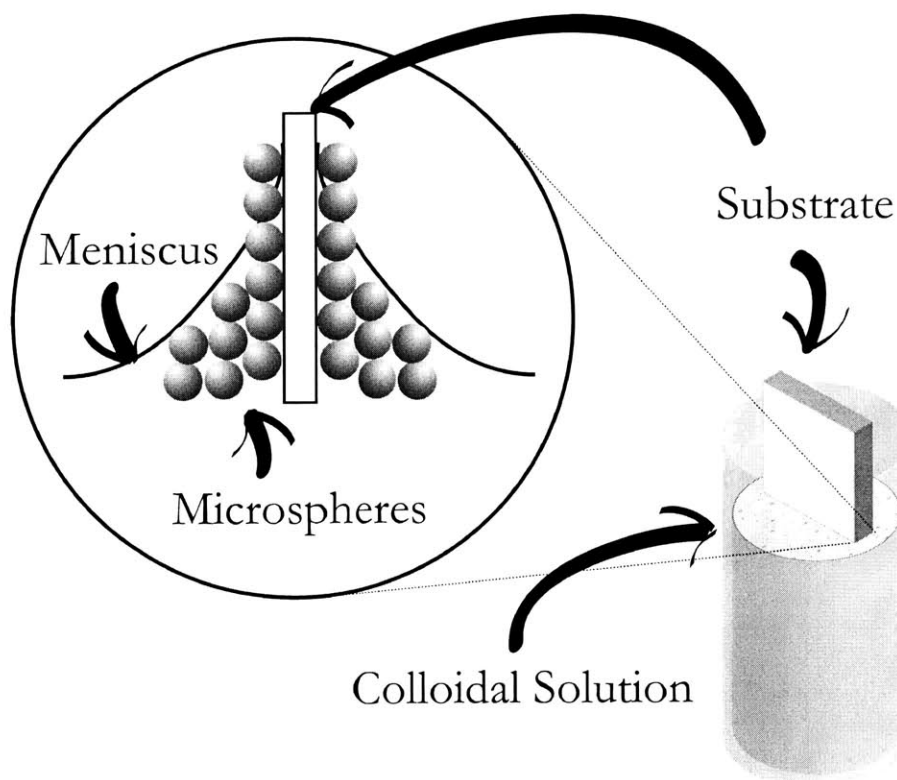

Figure 3.5. A schematic diagram of the vertical evaporation setup. The magnified view shows colloidal deposition process.

Vertical Evaporation

Evaporation is another simple deposition technique that has the advantage of requiring few steps and little equipment, however long evaporation times, lasting for several days, limit the usefulness of this technique. Figure 3.5 depicts a setup similar to the one used in the evaporation experiments. As can be seen from Figure 3.5, the cleaned substrates were placed vertically into a vial containing solutions of varying concentrations of spheres and solvents. Then, the vial is placed in an oven to speed the drying process. As the solvent evaporates, the surface tension between the solvent and the surface of the substrate forms a meniscus that forces microspheres to adhere to the surface of the substrate.

Electrically Guided Assembly

Using a technique pioneered by Aksay in the Department of Chemical Engineering in Princeton, colloidal suspensions are assembled into planar lattices using alternating current electric fields [14]. Close packed clusters or sparse arrays form depending on the frequency and relative particle concentrations. The frequency dependence of the assembly behavior is an interesting and complex relationship. At low frequencies (< 3 kHz) the microspheres repel each other and separate uniformly, creating a sparse lattice. At high frequencies (20-200 kHz) the microspheres attract one another and aggregate into large clusters. A schematic diagram of the experimental setup used to observe the microsphere formations in-situ is illustrated in Figure 3.6. While this technique presents the opportunity to fully control the placement of microspheres on a substrate, there is currently no method of depositing the spheres onto the substrate. As the solvent evaporates, the spheres aggregate and cluster at the boundaries of the

solution as they no longer are affected by the strong electric fields. At present, this technique is solely used to observe microsphere behavior in solution. If there existed a method to affix the spheres to the surface of the substrate while still being suspended by the electric fields, then this technique would be suitable for creating uniform monolayers appropriate for devices.
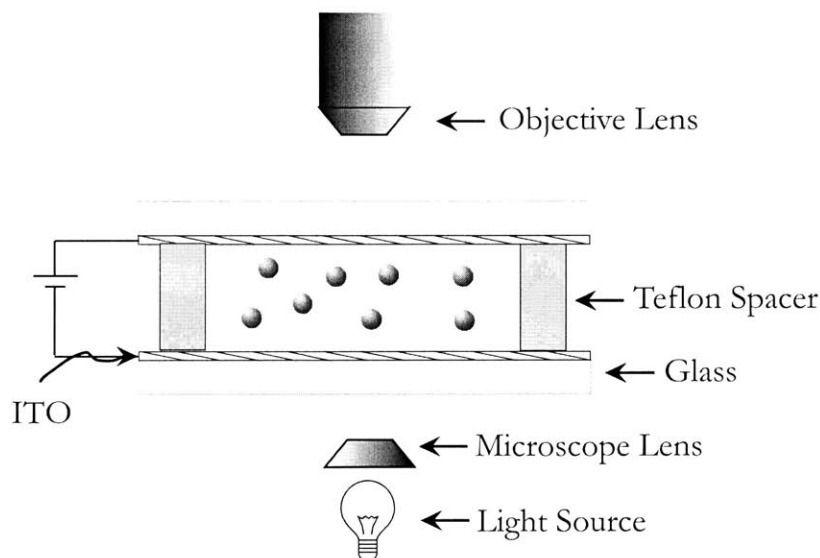
Figure 3.6. Schematic of the apparatus for pattern formation and in-situ observation. The ITO electrodes are separated with a 500 micron Teflon spacer.

Deposition of Metallic Nanoparticles

Gold and Silver nanoparticles have been observed to scatter visible light. To take advantage of this property in a working OLED device, I use an Angstrom Engineering Evaporation System to deposit thin (approximately 1 Å to 10 Å thick) films of gold or silver on top of the ITO electrode. Growing at a rate of 0.5 Å/sec allows me to accurately control the thickness of these thin films. The Angstrom Engineering system maintains a steady rate of growth through a computer-controlled feedback loop.

C h a p t e r   4

DISCUSSION AND RESULTS

Photolithography Results

I have experience fabricating three different interference patterns: lines, posts in a square lattice, and posts in a hexagonal lattice. Lines etched in silicon are the simplest pattern to fabricate because the substrate only requires one exposure. Both the square lattice and hexagonal lattice post formations require two exposures at 60% of the dosage of one regular exposure. Figure 4.1 1 displays a sample result from the Lloyd's Mirror Interferometer.
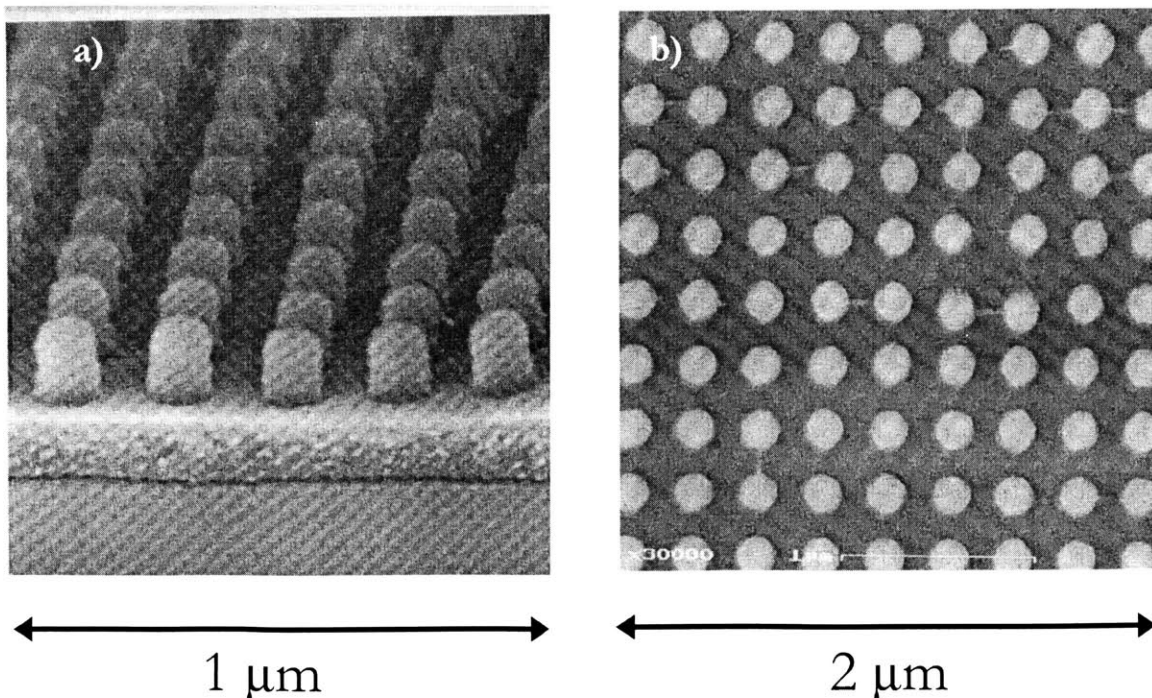

Figure 4.1. a) A cross-sectional view of a 340 nm square-post grating in PFI 88 positive photoresist on a stack of SiOx and Barli ARC (20 nm and 90 nm respectively). b) A top view of the same pattern.

Nanolithography Results

Figure 4.2 shows Atomic Force Microscopy (AFM) images of patterned, PDMS thin films.

$$10 \ \mu m \qquad\qquad 10 \ \mu m$$
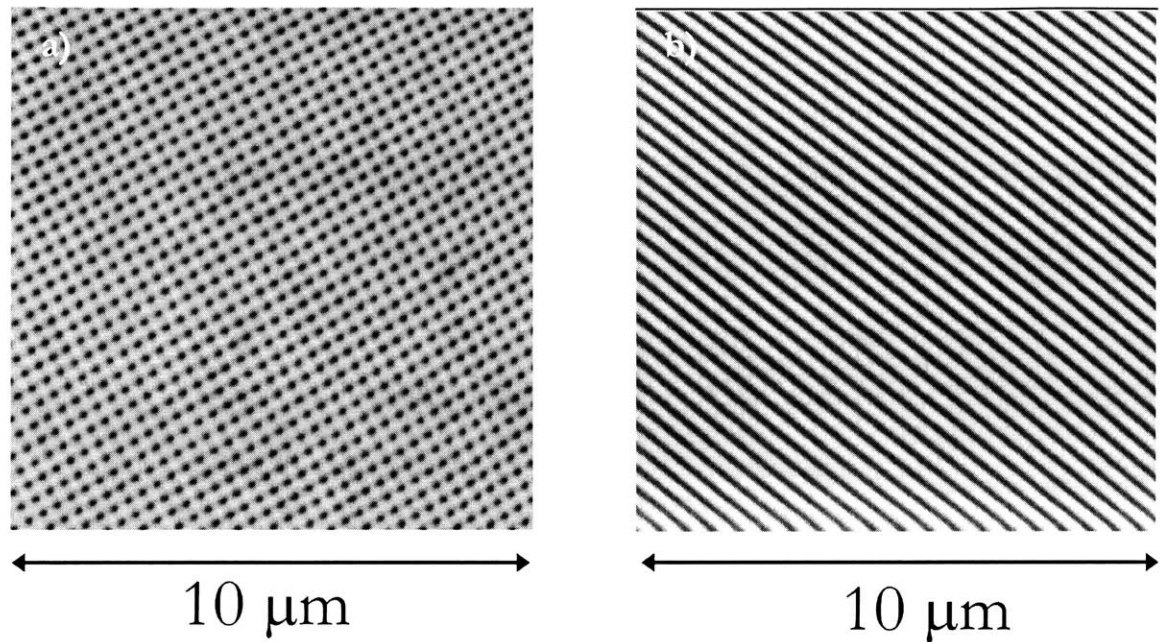
Figure 4.2. a) An AFM image of a square hole pattern in PDMS with 340 nm period. b) An AFM image of a 320 nm period grating of lines in PDMS.

In order to approach the limits of a true 2-D photonic bandgap material, the depth of the features in the PDMS must approach the thickness of the film. Typically, the PDMS films are around 7 microns. To get thinner films on the order of 3 microns, solutions of chloroform and PDMS can be used. However, pinholes and pores begin to show up in the PDMS films upon careful inspection with an AFM (see Figure 4.3). This could be due to chloroform that remains trapped in the PDMS during the curing process. As the PDMS cures, the trapped chloroform would begin to evaporate try to escape the PDMS, causing bubbles in the film.

Figure 4.3. a) An AFM image of a 320 nm period grating with pinholes. b) An AFM image of a 320 nm period square post pattern with larger pinholes.
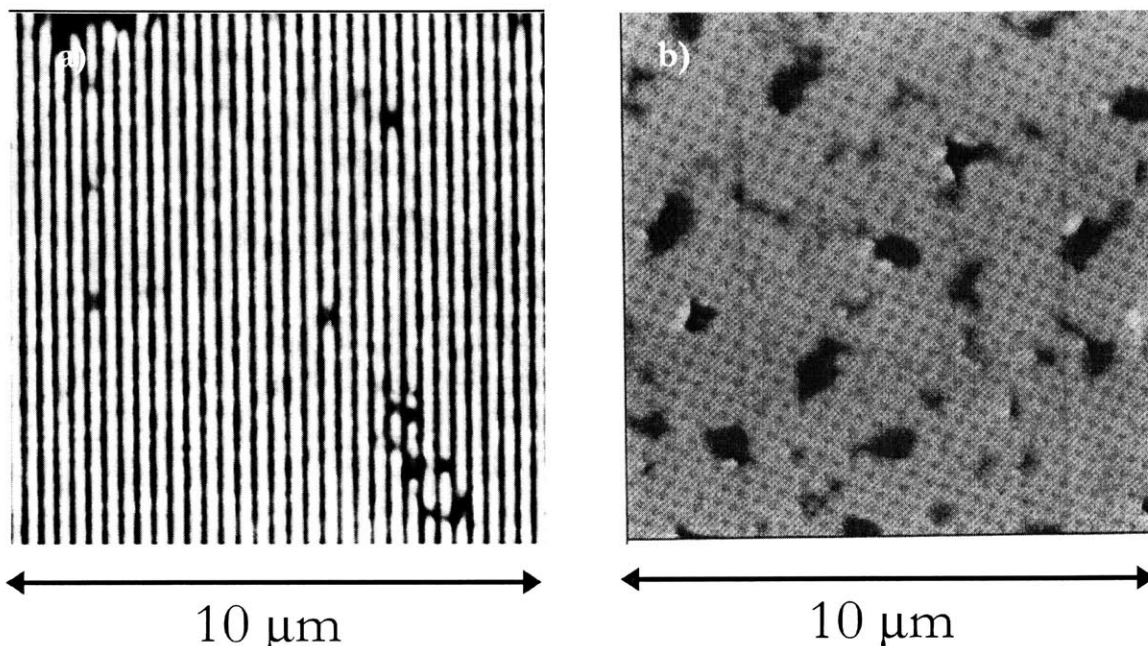
An alternate solution to fabricate deeper features is to make the pattern features large enough to make up for the microns thick PDMS films. However, there is a tradeoff between the rigidity of the nanopatterned features, in PDMS and silicon, and their aspect ratios. Tall and thin silicon features may be so fragile that they would not withstand the applied forces of patterning and stamp removal from the soft lithography processing. Furthermore a tall PDMS feature has a greater tendency to collapse upon itself as can be seen in Figure 4.3.

More work remains to be done in refining the soft lithography techniques mentioned above with the ultimate goal being to achieve sub-micron thick, pinhole-free PDMS films with feature sizes in the nanometer range. Potential venues for future research include using a variation of PDMS with different curing properties that would allow it to be diluted with a solvent without affecting the pattern transfer process.

Colloidal Deposition Results

Figure 4.4 displays a few SEM images of different microsphere-coated samples. From the images in Figure 4.4, it is possible to see that there are many defects that would cause electrical shorts in devices such as clustering and bare areas. Changing spin speeds did not yield any noticeable trends. Also, using different solvents did not yield any clear distinctions between samples. However, the concentration of spheres in the solutions did seem to have an effect on the coverage of the samples. Yet, from the small set of data collected, it is difficult to make any definite generalizations. From the data collected, spin-casting appears to be an appropriate deposition technique when a uniform, monolayer of microspheres is not strictly required.

Outcomes from vertical evaporation experiments yielded a qualitatively more uniform and flat microsphere layer. However, the excessive drying times make this technique an unwieldy process. An improvement over the existing vertical evaporation technique would be to slowly draw out the substrate at a steady rate. This technique might help to speed up the evaporation process while maintaining the uniformity that comes from evaporation. Devices with an integrated microsphere layer have been fabricated; however, no reliable data could be measured due to shorts caused by the large height changes within the sputtered ITO layer that lay on top of the microsphere layer. One possible solution to this problem is to deposit an optically transparent, electrically inactive layer (i.e. parylene) on top of the sputtered ITO layer to smooth out any drastic changes in layer depth. Figure 4.5 shows the SEM results of the parylene-coated samples, but working devices have yet to be fabricated.

5% .33µm Silica Microspheres
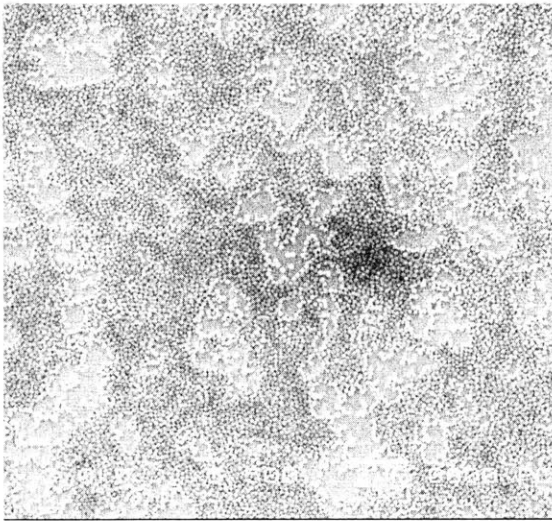
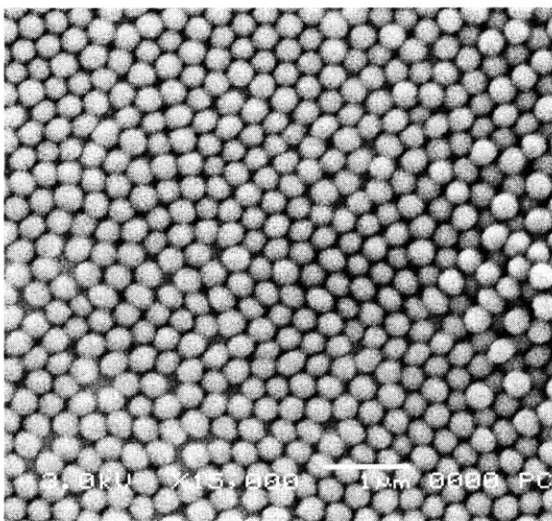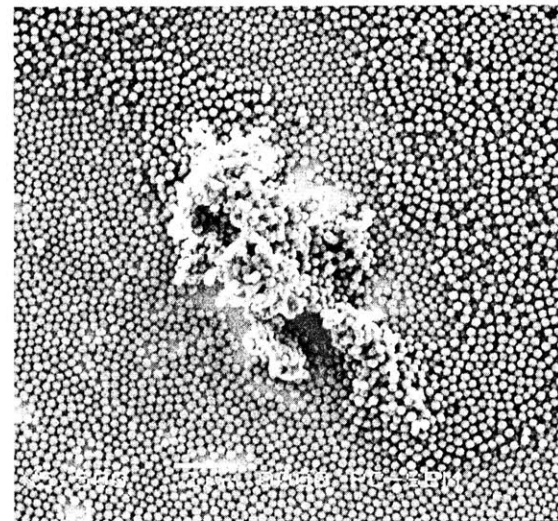2000 RPM   3000 RPM
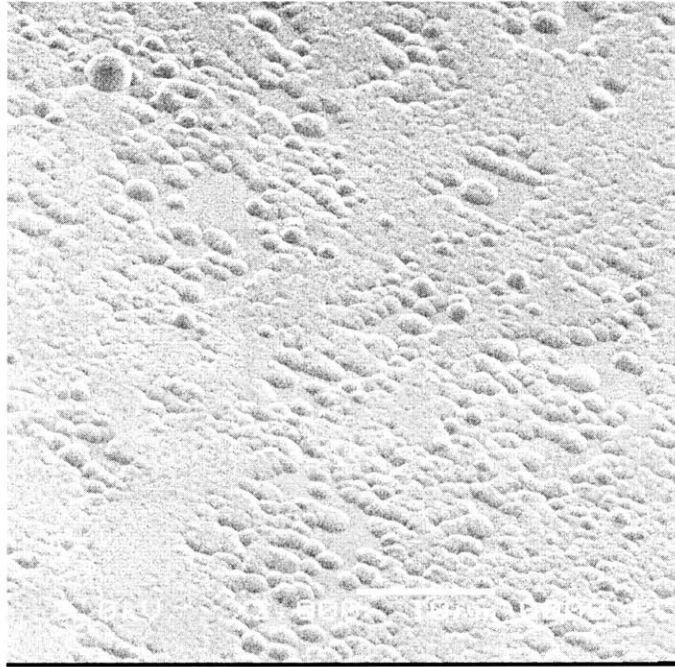
10% .33µm Silica Microspheres

2000 RPM   3000 RPM

Figure 4.4. SEM images of different microsphere depositions at magnifications of a) 5, 500X, b) 1000X, c) 15,000X, d) 5,500X.

Figure 4.5. An SEM image (taken at a magnification of 2000X) of a microsphere-coated sample with a 1 micron layer of parylene on top. The image was taken at an angle of 45 degrees from the normal to emphasize the flatness of the surface.

The scattering properties of a roughened ITO surface have been simulated using BeamProp [15], an integrated Computer-Assisted Design and simulation program for waveguides and fiber optics. We want to understand how light in a device similar to the one illustrated in Figure 2.6 behaves. First, we can simplify the analysis by considering only the cathode, the organic layer, the ITO layer, and some lower index of refraction substrate (in this case parylene) for the simulation. BeamProp allows us to find the fundamental mode profile of the structure, and Figure 4.6 shows sample data from BeamProp that illustrates how the light prefers to travel in the ITO layer based on its high index of refraction.
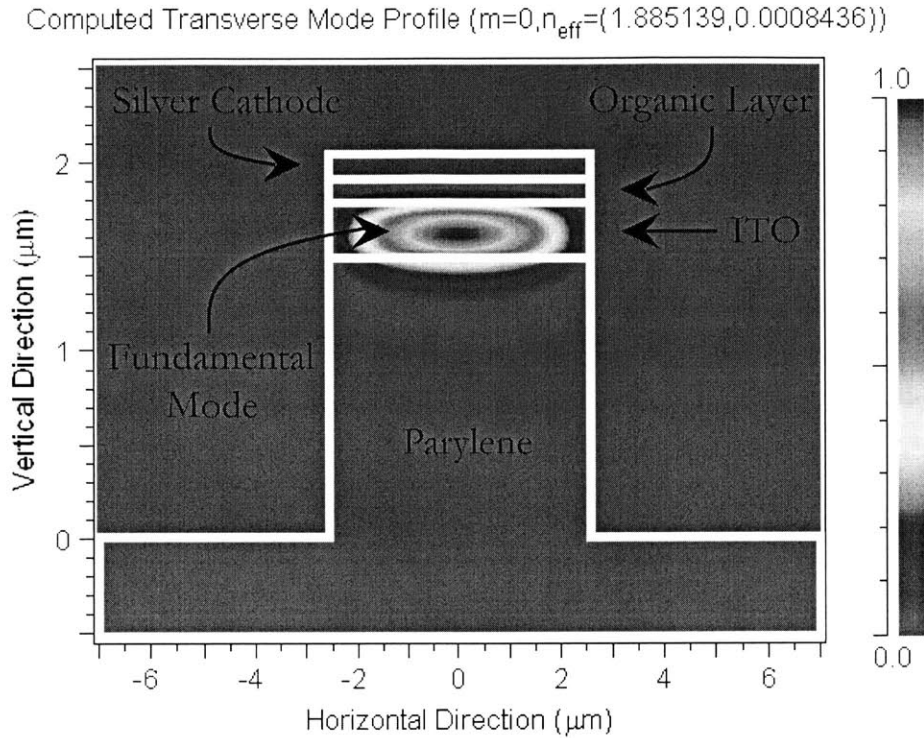
Figure 4.6. Sample fundamental mode simulation (λ = 530 nm) from BeamProp with an overlay showing the following layers from top to bottom: 1) Ag cathode (n $\approx$ 0.25 + 3.5i, 100 nm), 2) Organic layer (n $\approx$ 1.7, 100 nm), 3) Sputtered ITO (n $\approx$ 2.0, 250 nm), 4) Parylene (n $\approx$ 1.66, 1500 nm).

Once the fundamental mode information is established, we can launch a beam of light (Gaussian profile) from within the ITO layer and monitor its power as a function of distance traveled in the layer. BeamProp has the functionality to include absorption effects and scattering from "lithographic roughness" on the sidewalls of the waveguide structure. With these parameters, we can examine the effects that absorption from the cathode and scattering roughness (150 nm = radius of the microspheres) has on the power of the light as it travels through the ITO layer. Figure 4.7 plots the power as a function of distance traveled in the ITO layer for all of the combinations of absorption and scattering effects.
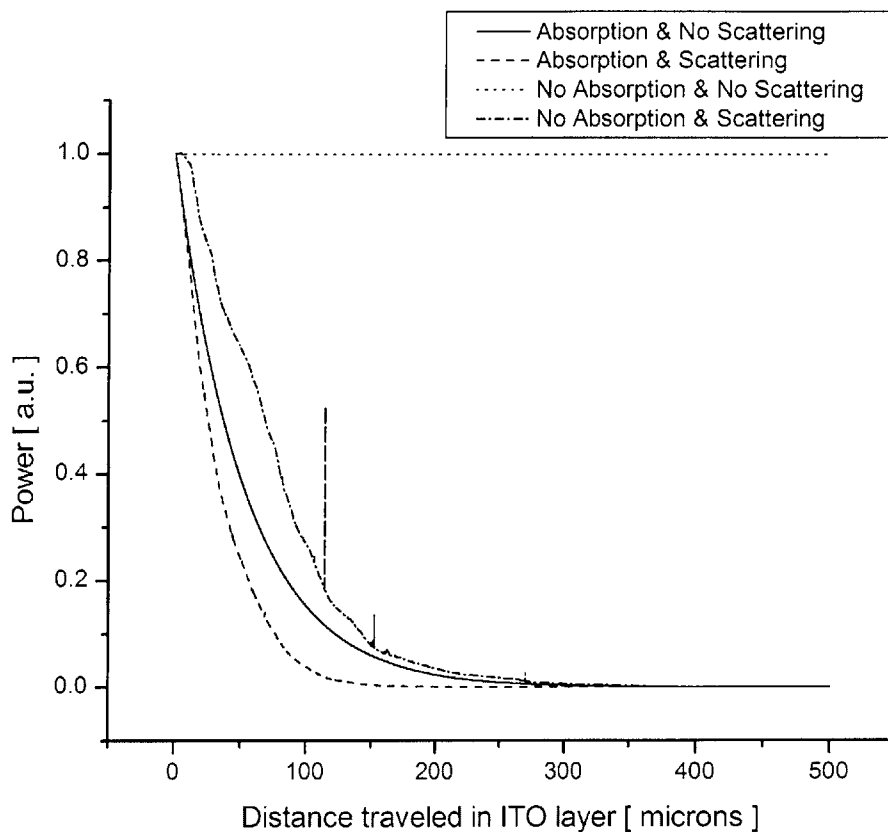
Figure 4.7. A comparison plot (power vs. distance traveled in the ITO layer) between all of the different combinations of loss mechanisms in the waveguide structure.

There is an important point to take away from this simulation. Even if we assume an absorptive cathode and scattering centers, light can travel in the ITO layer for over 100 microns. This very important piece of information allows us to make the approximation that all of the contributions from secondary reflections will eventually scatter almost all of the emitted light into the glass substrate, which verifies the major assumption made in the calculations to estimate the improvement in external extraction efficiency.

Metallic Nanoparticle Results

Devices have been fabricated with thin films of silver and gold under the assumption that the metal will pool into nanoparticles that will later act as the scattering centers in an OLED. Figure 4.8 displays quantum efficiency data from an OLED with 5 Å of silver deposited on top of the ITO layer. Clearly, the OLEDs with 5 Å of silver deposited on top of the ITO layer all exhibited lower external quantum efficiencies than their conventional OLED counterparts.
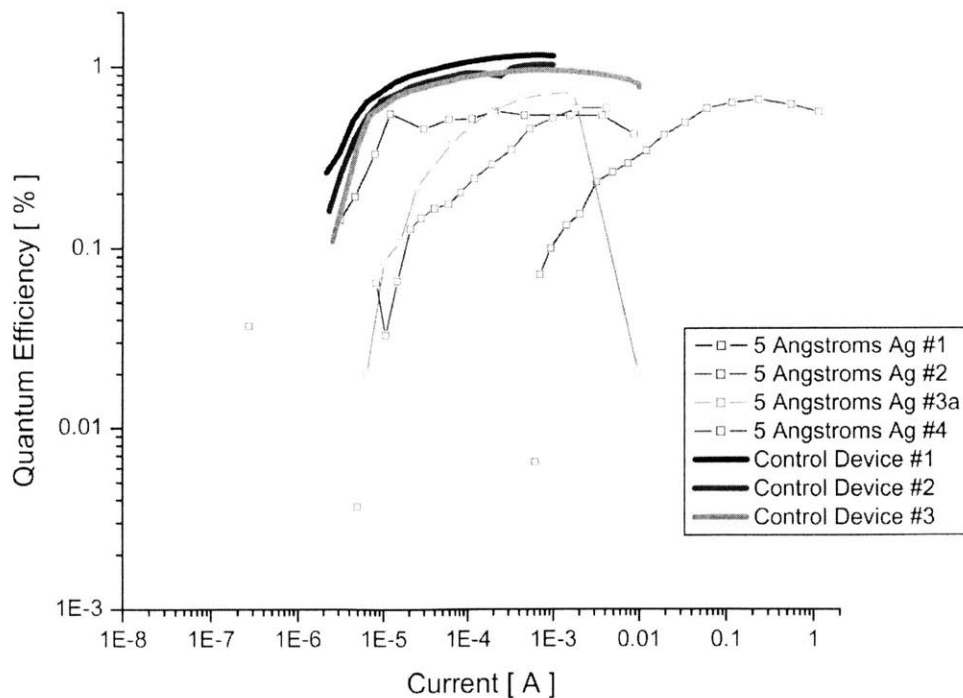

Figure 4.8. An external quantum efficiency vs. current plot of conventional and Ag nanoparticle green OLEDs.

It is possible that the external quantum efficiency of the devices with the silver layer decreased because of the high work function of silver (W ≈ 4.3 eV), which creates a large barrier at the

cathode for electron injection. In addition, silver can readily oxidize during thermal evaporation and create a thin, insulating layer covering the ITO anode, thus diminishing device performance. Therefore, gold nanoparticles have become the next best choice for creating scattering nanoparticles. Figure 4.9 compares the device characteristics of conventional, green OLEDs to devices that contain a 10 Å gold nanoparticle film on top of the ITO layer.

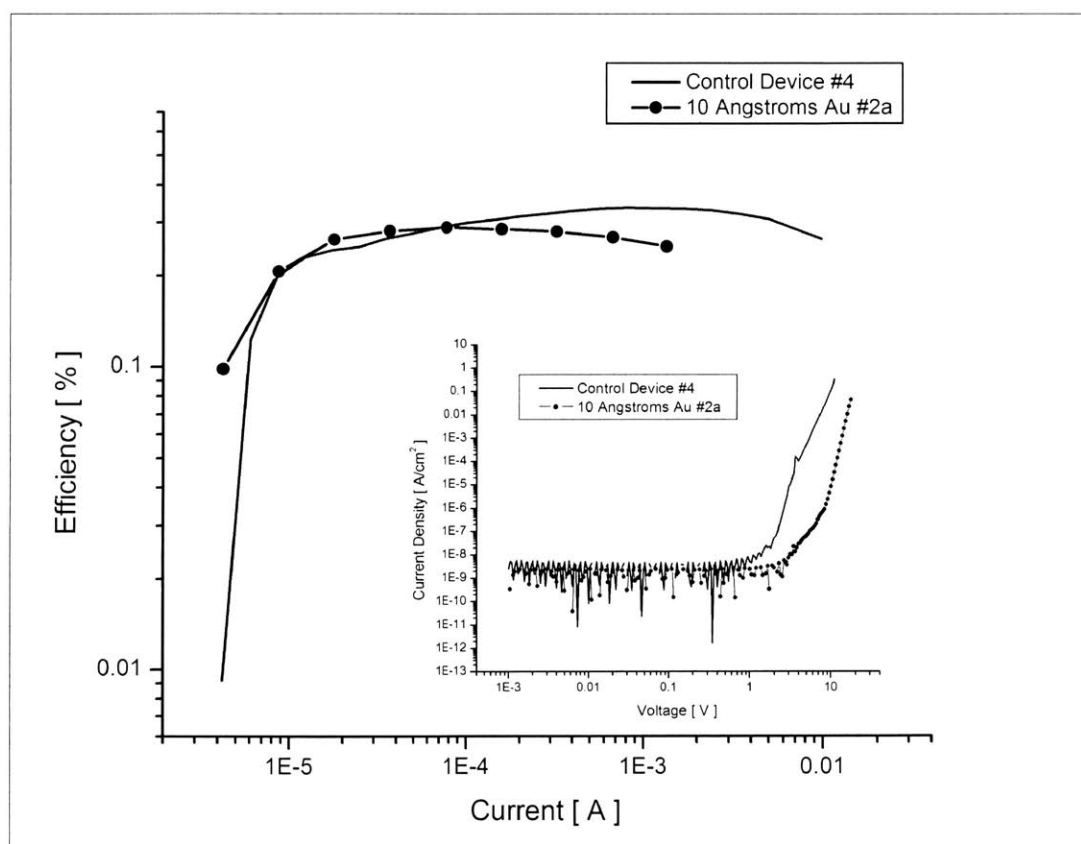**Figure 4.9. An external quantum efficiency vs. current plot of conventional and Au nanoparticle green OLEDs.**

At present it is not understood exactly why the devices with 10 Å of gold are performing worse than conventional OLEDs. In order to have a better understanding of the effects of

adding a nanoparticle layer on top of the ITO anode, more work needs to be done on characterizing the metallic nanoparticle films.

Chapter 5

CONCLUSION

In this Master's Thesis, a number of approaches to improving outcoupling efficiency have been investigated and are still being explored. Primitive fabrication techniques and processes have been demonstrated and have been considered for applications in working devices. Through PDMS structures we may be able to create arrays of microlenses. With the microsphere deposition techniques we may be able to construct substrates that exhibit enhancement for outcoupling light. Metallic nanoparticles also look to be a promising venture for improving OLED efficiencies.

In order to realize an actual device that exhibits improvements in out-coupling efficiency, there are several challenging issues that need to be addressed: characterization of the effects of shape and size of gold nanoparticles on the scattering of different wavelengths of light, the effect of surface plasmon resonances on absorption losses, and methods of deposition for gold nanoparticles.

Future work will include developing numerical simulations using the light-scattering theory of spherical nanoparticles and ray-tracing techniques to determine the relationship between the size and shape of a nanoparticle to the wavelength of scattered light. Numerical modeling will also provide theoretical absorption spectra that will be important in characterizing the wavelengths of absorption for different surface plasmon resonances. In conjunction with the

simulations, I can continue to conduct experiments to verify the theoretical calculations. Distinct absorption profiles for different thicknesses of gold films can be leveraged to determine the relationship between the thicknesses of evaporated films to the average size of the nanoparticles. By comparing the experimental spectra with numerical simulations, I can begin to approximate the size and shape of the deposited nanoparticles. Atomic Force Microscopy (AFM) will also be useful in characterizing the gold films. However, the nanoparticles I will be working with will most likely be near the limits of resolution for the AFM. Thus, I will need to take into account the shape of the cantilever tip and the effect that it will have on the recorded images. There is commercial software available that can remove the artifacts of AFM tips from images, which will prove useful in acquiring more accurate size and shape information.

There is still much more work to be done in the area of optimizing OLED structure to increase device performance. As the search for the performance limits of OLEDs continues to fascinate researchers, new device structures will become more and more of a reality. This research lays the groundwork for fabricating novel device structures that will enhance the external extraction efficiency, which should prove to be a fruitful area for continued investigation.

BIBLIOGRAPHY

[1]   M. Pope, H. Kallmann, P. Magnante. "Electroluminescence of Organic Crystals."
J. Chem. Phys., Vol. 38, p. 2042, (1963).

[2]   W. Helfrich, W.G. Schneider. "Recombination Radiation in Anthracene Crystals." *Phys.
Rev. Lett.*, Vol. 140, p. 229, (1965).

[3]   C.W. Tang, S.A. Van Slyke. "Organic Electroluminescent Diodes." *Appl. Phys. Lett.*,
Vol. 51, p. 913, (1987).

[4]   J.H. Burroughes, et. al. "Light-emitting Diodes Based on Conjugated Polymers." *Nature*,
Vol. 347, p. 539, (1990).

[5]   P.E. Burrows, et. al. "Relationship Between Electroluminescence and Current Transport
in Organic Heterojunction Light-emitting Devices." *J. Appl. Phys.*, Vol. 79, p. 7991,
(1996).

[6]   M.A. Baldo, et. al. "Very High-efficiency Green Organic Light-emitting Devices Based
on Electrophosphorescence." *Appl. Phys. Lett.*, Vol. 75, p. 4, (1999).

[7]   G. Gu, et. al. "High-external-quantum-efficiency Organic Light-emitting Devices." *Opt.
Lett.*, Vol. 22, p. 396, (1996).

[8]   C.F. Madigan, M.H. Lu, J.C. Sturm. "Improvement of Output Coupling Efficiency of
Organic Light-emitting Diodes by Backside Substrate Modification." *Appl. Phys. Lett.*,
Vol. 76, p. 1650, (2000).

[9]   S. Moller, S.R. Forrest. "Improved Light Out-Coupling in Organic Light Emitting
Diodes Employing Ordered Microlens Arrays." *J. Appl. Phys.*, Vol. 91, p. 3324, (2002).

[10]   Y.J. Lee, et. al. "A High-extraction-efficiency Nanopatterned Organic Light-emitting
Diode." *Appl. Phys. Lett.*, Vol. 82, p. 3779, (2003).

[11]   M. Walsh. "Nanostructuring Magnetic Thin Films Using Interference Lithography." M.S.
Thesis, MIT (2000).

[12]   Y.N. Xia, G.M. Whitesides. "Soft Lithography." *Angew. Chem. Int. Ed.*, Vol. 37, p. 551,
(1998).

[13]   D.R. Lide. <u>CRC Handbook of Chemistry and Physics 81st ed.</u> *CRC Press*, 2000, p. 12-140.

[14] I.A. Aksay, et. al. "Field-induced Layering of Colloidal Crystals." Science, Vol. 272, p. 706, (1996).

[15] Developed by RSoft Design Group, Inc.